RESEARCH ARTICLE

BATTERIES

Solvation sheath reorganization enables divalent metal batteries with fast interfacial charge transfer kinetics

Singyuk Hou[1]†, Xiao Ji[1]†, Karen Gaskell[2], Peng-fei Wang[1], Luning Wang[2], Jijian Xu[1], Ruimin Sun[1], Oleg Borodin[3]*, Chunsheng Wang[1]*

Rechargeable magnesium and calcium metal batteries (RMBs and RCBs) are promising alternatives to lithium-ion batteries because of the high crustal abundance and capacity of magnesium and calcium. Yet, they are plagued by sluggish kinetics and parasitic reactions. We found a family of methoxyethyl-amine chelants that greatly promote interfacial charge transfer kinetics and suppress side reactions on both the cathode and metal anode through solvation sheath reorganization, thus enabling stable and highly reversible cycling of the RMB and RCB full cells with energy densities of 412 and 471 watt-hours per kilogram, respectively. This work provides a versatile electrolyte design strategy for divalent metal batteries.

Energy upgrades and the implementation of electric transportation demand electrochemical storage systems with higher accessibility, energy density, and safety (*1*). Rechargeable divalent metal batteries, including rechargeable magnesium and calcium metal batteries (RMBs and RCBs), are appealing alternatives to lithium-ion batteries (LIBs) because of the crustal abundances of Mg and Ca, which are more than 1000 times that of Li; larger anode capacity from two-electron transfer (3832 mA·hours cm^{-3} for Mg and 2052.6 mA·hours cm^{-3} for Ca) (*2*); low reduction potential of Mg and Ca metal [−2.38 V versus standard hydrogen electrode (SHE) for Mg and −2.76 V versus SHE for Ca]; and reduced safety concerns from the potentially dendrite-free plating of Mg metal anode (*3*). To fabricate RMBs and RCBs with energy densities comparable to or higher than that of commercial LIBs, the metal anodes need to be paired with cathodes with a potential of >2.5 V versus Li$^+$/Li (fig. S1 and table S1), which necessitates the use of high-voltage metal oxide cathodes (*4*).

In LIBs, a Li$^+$ desolvates and transports through the electron-insulating solid-electrolyte interphase (SEI) to the electrode materials (*5, 6*).

[1]Department of Chemical and Biomolecular Engineering, University of Maryland, College Park, MD 20740, USA. [2]Department of Chemistry and Biochemistry, University of Maryland, College Park, MD 20742, USA. [3]Battery Science Branch, Sensors and Electron Devices Directorate, US Army Combat Capabilities Development Command Army Research Laboratory, Adelphi, MD 20783, USA.
*Corresponding authors: cswang@umd.edu (C.W.); oleg.a.borodin.civ@army.mil (O.B.)
†These authors contributed equally to this work.

Fig. 1. Overpotentials and CEs of Mg plating and stripping in different electrolytes.
(**A**) The molecular structure and denticity of the chelants. (**B** and **C**) The overpotentials at the 10th cycle for plating and stripping in Mg||Mg cells at (B) 1.5 mA cm^{-2} for 1.5 mA·hours cm^{-2} and (C) 0.1 mA cm^{-2} for 0.1 mA·hours cm^{-2} in the blank and **Ex**. (**D**) CEs for Mg plating and stripping in **Ex** in Mg||SS cells cycled at 0.1 mA cm^{-2}. (**E**) Long-term cycling of the Mg||SS cell in **E4** at a current density of 0.1 mA cm^{-2}.
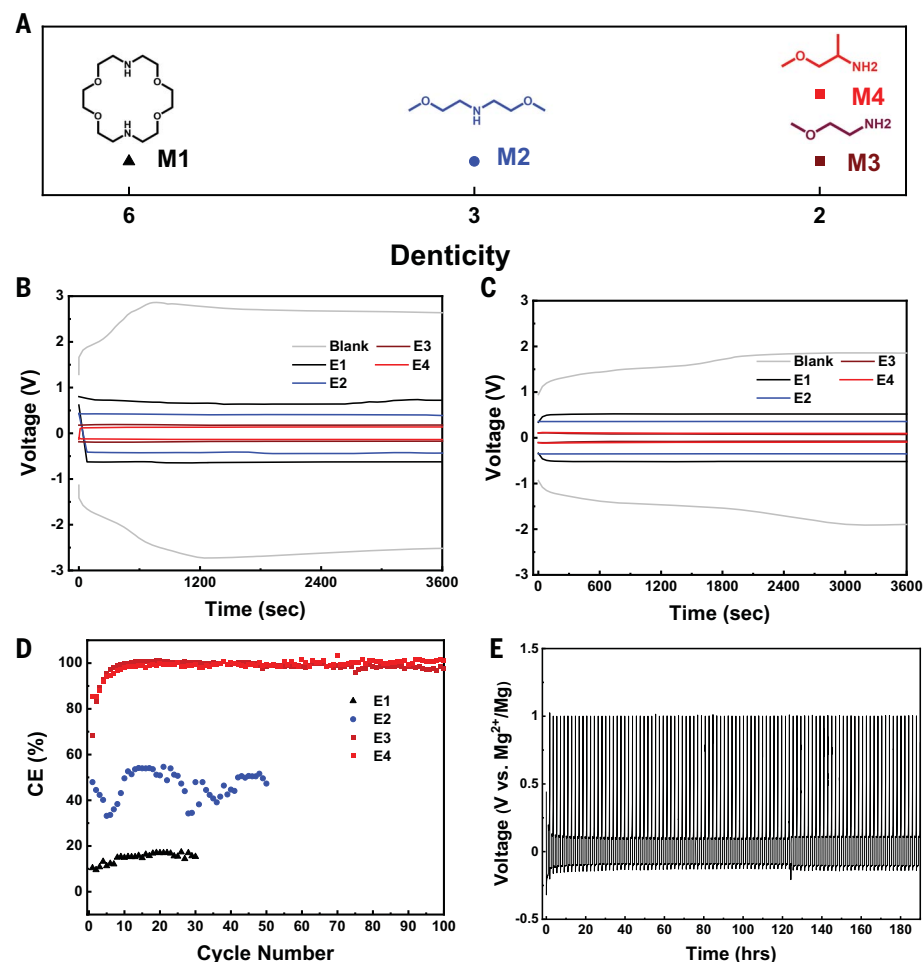
Desolvation and transport of the divalent ions through SEI and active materials, however, are more challenging owing to stronger electrostatic interactions (7–12), leading to large overpotentials, electrolyte decomposition (8, 9), and irreversible phase transformations or failure to intercalate in cathode materials (13–15). Reductive and chloride-containing nonaqueous electrolytes avoid SEI formation on Mg anodes but suffer from low anodic stability and incompatibility with current collectors and battery casings (16–18). Aqueous electrolytes assist Mg^{2+} intercalation in high-voltage cathodes (14, 15, 19, 20) but do not support reversible metal anodes (16, 17). To bridge the incompatibility among electrolytes to the cathode, anode, and current collectors, electrolytes consisting of noncorrosive electron-delocalizing anions, such as magnesium bis(trifluoromethanesulfonimide) [$Mg(TFSI)_2$] (21, 22), boron clusters (23–25), alkoxyborates and alkoxyaluminates (26–29), and an artificial SEI on a Mg anode, were reported (30). However, Mg and Ca anodes still suffer from insufficient coulombic efficiency (CE) while large hysteresis is observed on the cathode side.

We demonstrate that the multidentate methoxyethyl-amine chelants [–$(CH_2OCH_2CH_2N)_n$–] in the first solvation sheath of Mg^{2+} and Ca^{2+} enable both highly reversible Mg and Ca anodes as well as fast (de)intercalation of Mg^{2+} and Ca^{2+} into high-voltage layered oxide cathodes. These chelants demonstrate 6 to 41 times higher affinity for Mg^{2+} than traditional ether solvents, yet the chelant-rich solvation sheaths bypass the energetically unfavorable desolvation process through reorganization, thus reducing the overpotential and eliminating the concomitant parasitic reactions for both the anode and cathode. The reorganization energy of these electrolytes can be tuned by changing the dielectric constants and sizes of the chelants.

Results and discussion

Mg plating and stripping in chelating electrolytes

A 0.5 M $Mg(TFSI)_2$ in 1,2-dimethoxyethane (DME) electrolyte was adopted as the baseline (blank) because of its chemical stability and commercial accessibility. The proposed electrolytes are 0.5 M $Mg(TFSI)_2$ in DME-**Mx** (x = 1, 2, 3, or 4), in which **M1**, **M2**, **M3**, and **M4** are hexadentate, tridentate, and bidentate chelants for Mg^{2+} (Fig. 1A). The quantities of **Mx** are varied to keep the molar ratios between donor atoms in **Mx** to Mg^{2+} at 8:1 (materials and methods). These electrolytes are referred to as **Ex** (x = 1, 2, 3, or 4).

Mg plating and stripping overpotentials were evaluated in Mg||Mg symmetric cells at a variety of currents (fig. S2). Consistent with previous studies, the overpotentials are around 2.0 V in the blank (21) but are substantially reduced in **Ex**, dropping to below 0.1 V in **E4** (Fig. 1, B and C). Because the ionic conductivities of **Ex** (4.0 to 5.3 mS cm^{-1}) are smaller than that of the blank (6.5 mS cm^{-1}) (fig. S3), the reduced overpotentials in **Ex** are not attributed to bulk ion transport but rather to the interfacial charge transfer kinetics. As overpotentials reduce, the cycling CEs (cCEs, the average CE after 10 cycles) in Mg||stainless steel (SS) cells increase from 0% in the blank (owing to no Mg stripping at the cutoff potential of 1.0 V versus Mg^{2+}/Mg) to more than 99.5% in **E4** (Fig. 1D) with stable overpotentials (Fig. 1E and fig. S4) and dendrite-free Mg deposits (fig. S5).

The surfaces of the cycled Mg were characterized with high-resolution x-ray photoelectron spectroscopy (XPS). The decomposition products from DME and TFSI$^-$ are summarized in table S2. No signs of **Mx** decomposition are found in the N 1s spectrum (fig. S6). The species from electrolyte decomposition, in particular –C=O (C 1s and O 1s), crystalline $Mg(OH)_2$ (Mg 2p), –CF_x (F 1s), and –SO_x (x < 2, S 2p), and MgS_x (S 2p) are abundant on Mg cycled in the blank but diminish on Mg cycled in **Ex** (Fig. 2A). The decomposition layer is also much thicker in
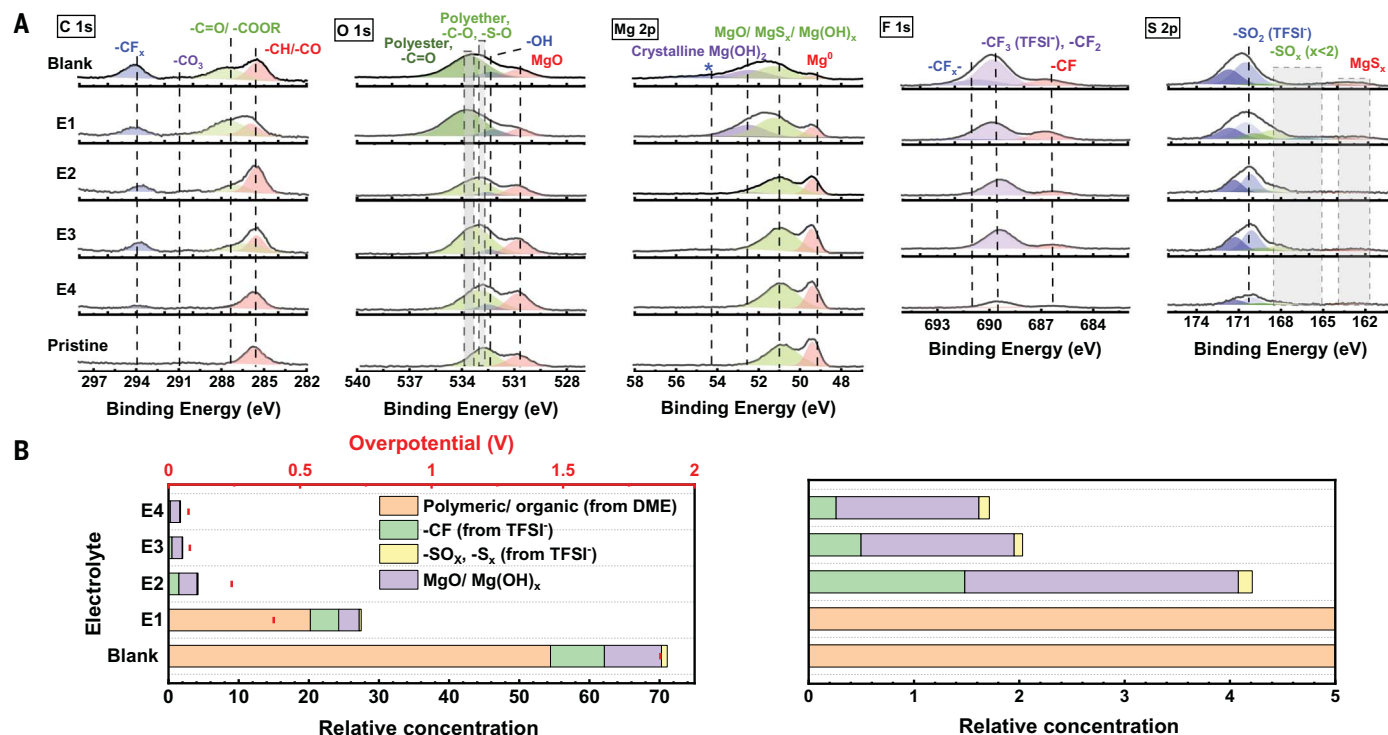
Fig. 2. Tailoring Mg surface composition with the chelants. (**A**) High-resolution XPS spectra of C 1s, O 1s, Mg 2p, F 1s, and S 2p of cycled (100 cycles at 0.1 mA cm^{-2}) and pristine Mg. For S 2p high-resolution XPS, only S 2p 3/2 were labeled; the unlabeled peaks are corresponding S 2p 1/2 spin split peaks. (**B**) The relative concentrations of decomposition species found on the cycled Mg surface. The peaks of –C=O in C 1s and O 1s are used to characterize polymeric and organic decomposition products from DME. All peak areas are normalized to those of Mg^0 to obtain relative concentrations. The red horizontal bars indicate the Mg plating and stripping overpotentials. The low relative concentration region is shown on the right.

the blank, as evidenced by the almost unchanged F and O accumulations after 12-min Ar⁺ sputtering (fig. S7). By contrast, the F and O accumulations on Mg cycled in **E3** and **E4** are negligible and can be removed with a much shorter sputtering time (fig. S7). The relative concentrations of these decomposed species show substantial dependence on the overpotentials (Fig. 2B). Thus, by reducing the overpotentials for Mg plating and stripping, electrolyte decomposition is suppressed and cCE is enhanced in **Ex**.

Solvation sheath structure

Without effective SEI, the solvation environment of Mg²⁺ serves as the key to understanding how **Mx** improves charge transfer kinetics of the Mg anode, which was probed using ¹³C nuclear magnetic resonance (NMR). Chemical shifts of methylene carbons in DME (δ_{DME}) and **Mx** (δ_{Mx}) shift up-field in the presence of Mg(TFSI)₂ (Fig. 3A). These changes ($\Delta\delta_{DME}$ and $\Delta\delta_{Mx}$) reflect the stoichiometric average between bound and free states (supplementary text). Thus, a smaller $\Delta\delta_{DME}$ in **Ex** indicates that DME is partially freed from the solvation

sheath (Fig. 3A, left). Meanwhile, the substantial association of **Mx** in the solvation sheath is evidenced by values of $\Delta\delta_{Mx}$ that are >10 times greater than those of $\Delta\delta_{DME}$ (Fig. 3B). Using $\Delta\delta_{Mx}$ and $\Delta\delta_{DME}$, the relative affinities of **Mx**-Mg²⁺ over DME-Mg²⁺ interactions were quantified (table S3), in which **M1**, **M2**, **M3**, and **M4** show affinities that are 41, 12, 10, and 6 times greater with Mg²⁺ than with DME, respectively (Fig. 3B). Separate analysis of N and O stoichiometry through $\Delta\delta_{Mx-N}$ (Fig. 3A, middle) and $\Delta\delta_{Mx-O}$ (Fig. 3A, right) ($\Delta\delta_{Mx}$ of carbon next to N and O, respectively) shows that the association of N in the solvation sheath greatly reduces from **E1** to **E4** (pink circles in Fig. 3B), but the association of O from **Mx** is, in general, greater than that from DME in the solvation sheath (Fig. 3B). Conversely, bond lengths calculated from molecular dynamics simulations show that Mg²⁺–N bonds in **Mx** are 0.2 to 0.3 Å shorter than those in monodentate amines (31, 32), whereas the Mg²⁺–O bond lengths remain the same for DME and **Mx** (figs. S8 to S10). Therefore, the higher affinity between **Mx** and Mg²⁺ is likely to be initiated by the strengthened Mg²⁺–N bonds

that in turn promote the Mg²⁺–O association. The formation of contact ion pairs (CIPs) between TFSI⁻ and Mg²⁺ was also characterized with Raman spectroscopy because CIPs potentially facilitate the decomposition of TFSI⁻ (33) and reduce anode reversibility. The S–N stretching vibration in TFSI⁻ that is sensitive to ionic interactions was deconvoluted to identify the solvent-separated ion pairs (SSIPs) and CIPs (Fig. 3C, fig. S11, and supplementary text). CIP percentages obtained by normalizing CIPs to total peak areas show that only 15 to 20% of the TFSI⁻ are in contact with the cations in both the blank and **Ex** (Fig. 3D). Thus, the major role of **Mx** is to displace DME instead of TFSI⁻ from the solvation sheath. Owing to the high affinity between **Mx** and Mg²⁺, the solvation sheaths containing **Mx** are more stable than the Mg²⁺(DME)₃ solvates in the blank by 0.3 to 1 eV (30 to 100 kJ mol⁻¹), as determined from density functional theory (DFT) calculations (Fig. 3E and figs. S12 and S13). **M1** has the strongest affinity to Mg²⁺ followed by **M2** and **M4** ≈ **M3**, in agreement with NMR results and molecular dynamics simulations.

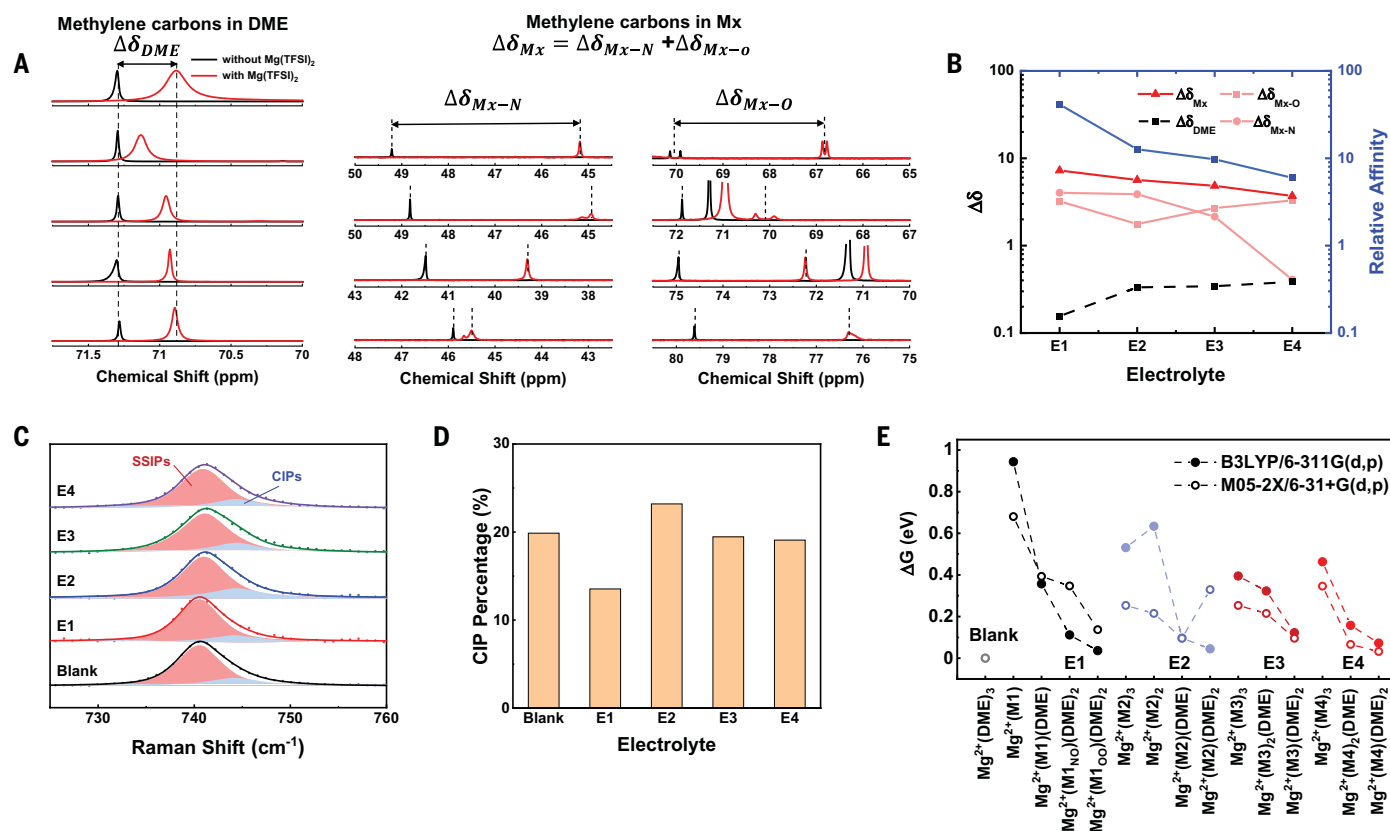**Fig. 3. Characterization of the Mg²⁺ solvation sheath in different electrolytes.** (**A**) ¹³C NMR spectra of methylene carbons in DME (left) and **Mx** (middle and right) with and without Mg(TFSI)₂. ppm, parts per million. (**B**) Summary of $\Delta\delta$ and the relative affinities of **Mx**-Mg²⁺ interactions compared with that of the DME-Mg²⁺ interaction. (**C**) Raman spectra for the S–N stretching vibration of TFSI⁻. The SSIPs and CIPs are fitted through a pseudo-Voigt function. (**D**) The percentage of TFSI⁻-forming CIPs with Mg²⁺ in the solvation sheath determined by the ratio between the CIP peak area and the total peak area from the Raman spectra. (**E**) The relative binding free energies (ΔG) for the Mg²⁺ solvates relative to Mg²⁺(DME)₃ from M05-2X/6-31+G(d,p) and B3LYP/6-311G(d,p) DFT calculations with polarized continuum model (ε = 7.19); higher values indicate more stable solvates.

Solvation sheath reorganization mediated charge transfer on the Mg anode

To understand why solvates in **Ex** with much higher binding energies than those in the blank (Fig. 3E) support Mg plating and stripping with smaller overpotentials, the electron transfer from an electrode to solvated Mg^{2+} was analyzed. It is approximated as nonadiabatic (*34*), involving ionic intermediates with the reorganized solvation sheath according to Marcus theory (*35*). For an electrode-bound electrochemical reaction, the overpotential (η) represents the potential required to vary the Fermi level (E_F) of the electrode for each electron transferred (*36*) and the reorganization energy (λ) represents the energy to reorganize the solvation sheath to accept the electron (Fig. 4A). The values of λ were obtained by fitting the Tafel plots for the Mg anode with

Marcus-Hush-Chidsey kinetics (*37, 38*) (equation S2 in fig. S14). To minimize interference from the morphological difference of Mg deposits and the electrolyte decomposition during Mg plating, only the stripping overpotentials of the freshly polished Mg were collected for fitting (fig. S14). The fitted λ showed distinct correlations with the η in three regions, marked as I, II, and III in Fig. 4B. Reactions in **E3** and **E4** fall into region I, in which λ for Mg^{2+} redox is considerably smaller than the onset of decomposition potential (E_D), resulting in little electrolyte decomposition (Fig. 2), and the η agrees well with the λ, reflecting that the electrons are transferred reversibly to Mg^{2+}; reactions in **E2** and **E1** fall into region II, in which λ overlaps with E_D and the η slightly deviates from the postulated λ for Mg^{2+} redox, reflecting that some side reactions take place;

and reactions in the blank fall into region III, in which the λ is larger than E_D and the η greatly deviates from the postulated λ for Mg^{2+} redox because the major reaction is now dominated by electrolyte decomposition (Fig. 4B).

The solvation sheath reorganization energy (λ) can be expressed as a dielectric continuum formulation:

$$\lambda = \frac{e^2}{4\pi\varepsilon_0}\left(\frac{1}{a_0} - \frac{1}{R}\right)\left(\frac{1}{\varepsilon_{op}} - \frac{1}{\varepsilon_s}\right)$$

where ε_0 is the vacuum permittivity, e is electron charge, a_0 is the solvated radius of the cations, R is the distance between the solvated ions and electrode surface, ε_{op} is the optical dielectric constant, and ε_s is the static dielectric constant (*39*), in which the λ
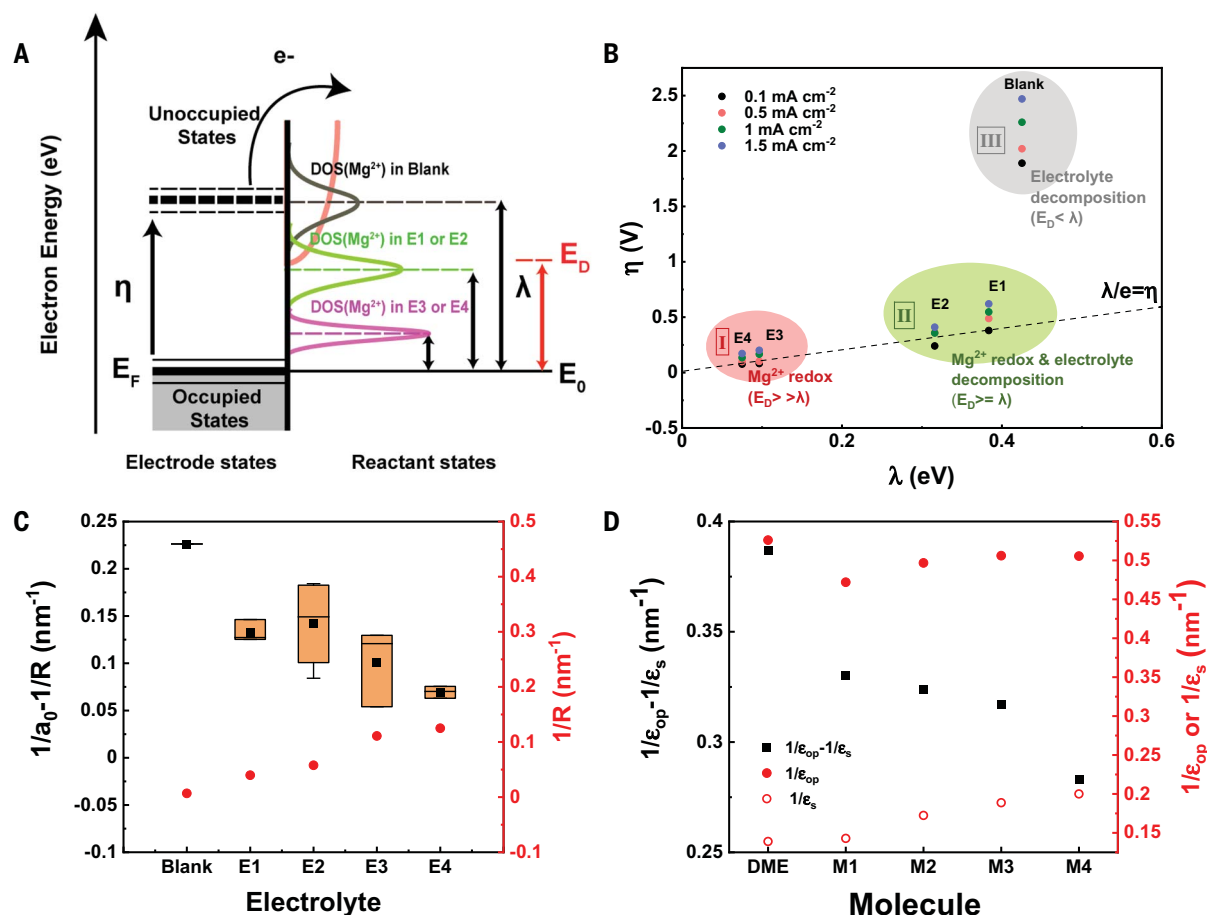

Fig. 4. Reorganization of the solvation sheath. (**A**) The Marcus-Gerischer diagram of electron transfer at the metal electrode–electrolyte interface. E_F refers to the Fermi level of the metal electrode, and E_0 refers to the energy level of the electrolyte and electrode at equilibrium. The red, green, and black Gaussians represent the density of state (DOS) of Mg^{2+} in the electrolyte. The orange curve represents the DOSs of other electrolyte components, and E_D refers to the onset potential of the electrolyte decomposition. (**B**) The correlation between overpotential (η) and reorganization energy (λ) for different reaction modes of the Mg anodes. The dashed line represents when the λ for electron transfer is equal to η. (**C**) The reciprocal of the distance between solvated ion and electrode surface $1/R$ (red dots) and the reciprocal of the distance part ($1/a_0 - 1/R$) in different electrolytes (box plot). Owing to multiple solvation radii ($1/a_0$) in each electrolyte, a box plot is used to account for the distribution of ($1/a_0 - 1/R$) between the first and the third quartile; the mean values of ($1/a_0 - 1/R$) are marked with black squares. (**D**) The reciprocal of the optical dielectric constant ($1/\varepsilon_{op}$) (red solid circles), static dielectric constant ($1/\varepsilon_s$) (red open circles), and dielectric part ($1/\varepsilon_{op} - 1/\varepsilon_s$) (black squares) for DME and **Mx**.
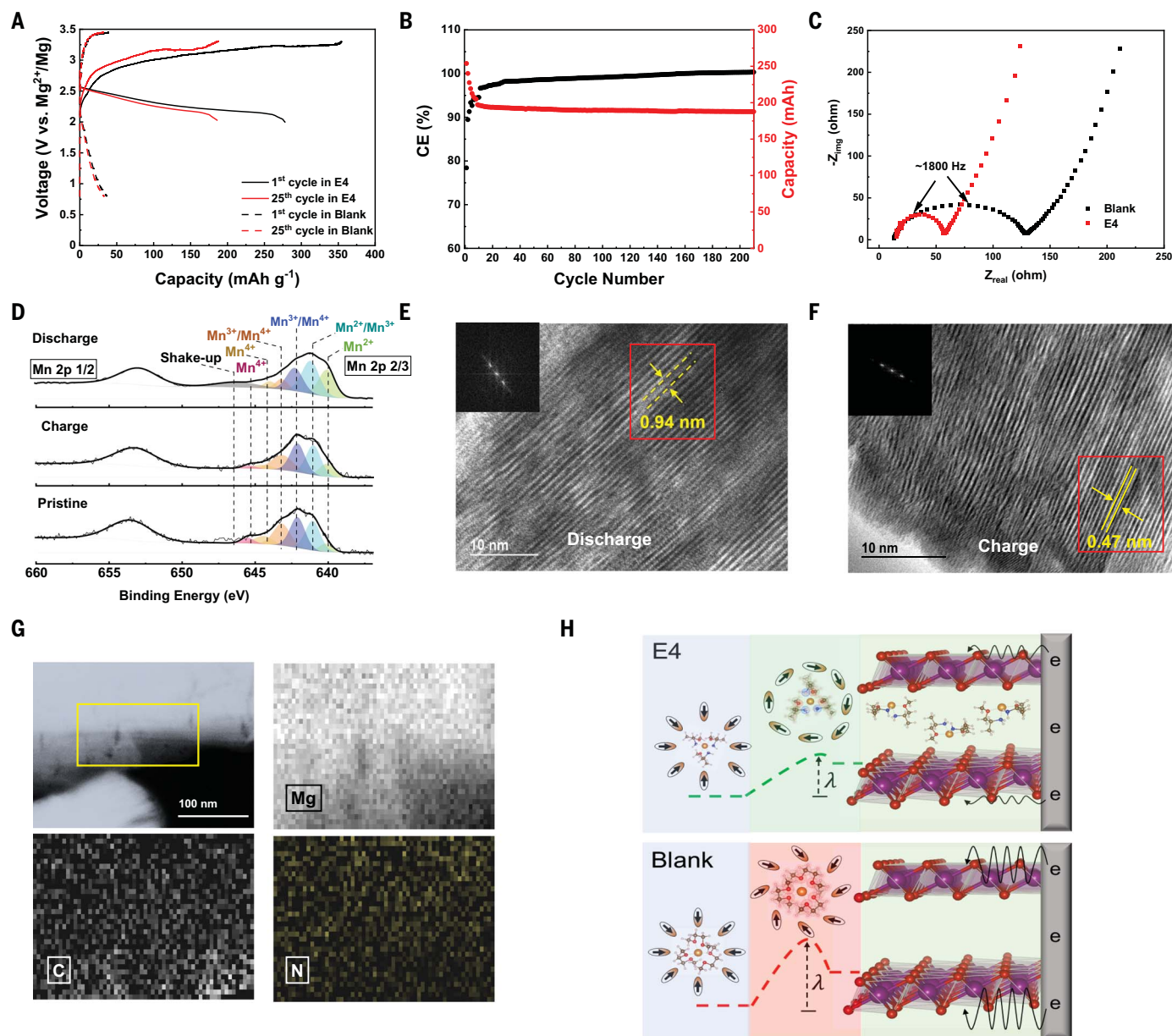
Fig. 5. Intercalation of Mg^{2+} and chelant in layered oxide. (**A**) The charge-discharge curve of the Mg$_{0.15}$MnO$_2$||Mg cell in **E4** and the blank at 0.5C (1C = 200 mA g^{-1}). (**B**) The capacity and CE of Mg$_{0.15}$MnO$_2$||Mg cycled in **E4** at 0.5C. (**C**) Electrochemical impedance spectra for Mg$_{0.15}$MnO$_2$ at a 0% state of discharge in the three-electrode cell after 25 cycles in the blank and **E4**, with a Mg counter electrode and magnesiated Mo$_6$S$_8$ reference electrode. EIS was measured between 10^6 and 0.1 Hz, with an ac oscillation of 10 mV amplitude. (**D**) Characterization of the Mn oxidative state with Mn 2p 3/2 high-resolution XPS spectra of discharge, charge, and pristine Mg$_x$MnO$_2$. (**E** and **F**) Transmission electron microscopy (TEM) image of Mg$_{0.15}$MnO$_2$ after (E) discharge (Mg^{2+} intercalation) and (F) charge (Mg^{2+} disintercalation) at the 25th cycle. The insets are the diffraction patterns from fast Fourier transformation of the marked area. (**G**) Scanning TEM (STEM)–EDX spectroscopy mappings of the elemental distributions of Mg, N, C, and O in the discharged Mg$_x$MnO$_2$ at the 25th cycle. (**H**) The scheme of concerted ion and electron transfer in the cathode host limited by the solvation sheath reorganization.

is proportional to the distance part $\left(\frac{1}{a_0} - \frac{1}{R}\right)$ and the dielectric part $\left(\frac{1}{\varepsilon_{op}} - \frac{1}{\varepsilon_s}\right)$. The distance part gradually reduces from the blank to **E4** (Fig. 4C) owing to a less compact solvation sheath (smaller $1/a_0$ except for **M3**; table S4). In addition, the formation of decomposition products during cycling increases the distance between the solvated ion and electrode R (Fig. 4C, fig. S15, table S5, and supplementary text).

This leads to an increase in λ. The dielectric part also reduces progressively from the blank to **E4** (Fig. 4D and table S6). Considering that $\frac{1}{\varepsilon_{op}}$ and $\frac{1}{\varepsilon_s}$ represent fast and slow solvent motions upon electron transfer (40), respectively, the smaller difference demonstrated by **Mx** suggests that the asymmetric chelants provide more polarizable environments compared with DME. To summarize, the less compact and

more polarizable solvation sheath reduces the λ for electron transfer, which consequently reduces overpotential by preventing electrolyte decomposition and promoting stable Mg plating and stripping.

In addition to the λ, substantial differences were observed for the initial Mg^{2+}/Mg$^+$ reduction potentials for the Mg^{2+}(**M4**)$_3$ and Mg^{2+}(DME)$_3$ solvates (figs. S16 to S18 and

table S7), with Mg^{2+}/Mg^+ reduction most readily occurring in $Mg^{2+}(\mathbf{M4})_3$, whereas reduction of $Mg^{2+}(DME)_3$ required a much larger overpotential by 0.4 to 0.6 V. An intermediate reduction potential is observed for $Mg^{2+}(\mathbf{M1})(DME)$ (fig. S16F) that is consistent with the intermediate performance of the **E1** electrolyte (Fig. 1, B to D). The larger overpotential to initiate electron transfer in the blank likely contributes to the slower interfacial kinetics and electrolyte decomposition. Because MgO is often present on Mg metal, solvent reactivity with MgO was examined in DFT calculations and it was found that the defect-free surfaces are not reactive toward DME or chelants (fig. S19 and table S8).

The solvation sheath mediated charge transfer in the layered oxide cathode

On the anode, the solvation sheath reorganized to the activated state at which the electron transfer occurred. In the oxide cathode, however, the ion accepts an electron indirectly through concerted intercalation near the transitional metal center, yet we found that the $\mathbf{M}x$ in electrolyte can also improve the charge transfer kinetics on the cathode. Mg-pillared layered MnO_2 ($Mg_{0.15}MnO_2$) was used as the cathode material, and **E4** was used to evaluate the electrochemical performance of the $Mg||Mg_{0.15}MnO_2$ cell owing to its higher anodic stability (3.8 V versus Mg^{2+}/Mg) (fig. S20). The $Mg||Mg_{0.15}MnO_2$ cell was charged-discharged between 2 and 3.3 V (versus Mg^{2+}/Mg) at 0.5C (1C corresponds to a 200 mA g^{-1} active material), and a reversible capacity of 190 mA·hours g^{-1} was achieved and maintained for 200 cycles (Fig. 5, A and B). Contrary to the performance in **E4**, the charge-discharge of the $Mg||Mg_{0.15}MnO_2$ cell in the blank showed little capacity at the same C-rate (Fig. 5A). Charge transfer resistances (R_{ct}) of the $Mg_{0.15}MnO_2$ cathode in the blank and **E4** were measured using electrochemical impedance spectroscopy (EIS) in a three-electrode cell with magnesiated Mo_6S_8 reference electrodes (Fig. 5C) to exclude potential variation from the Mg metal reference (fig. S21). The charge-transfer processes of the $Mg_{0.15}MnO_2$ cathode in **E4** and the blank are represented by the semicircles in the EIS spectra with similar characteristic frequencies. The values of R_{ct} determined by the diameters of the semicircles are two to three times smaller in **E4** than in the blank (Fig. 5C), suggesting a much faster charge transfer kinetics.

We further characterized the $Mg_{0.15}MnO_2$ cathode to identify the cause of faster charge transfer kinetics in **E4**. The reversible electron transfer to the $Mg_{0.15}MnO_2$ cathode was demonstrated by manganese (Mn) 2p 3/2 high-resolution XPS spectra, in which the peaks associated with Mn^{4+} reduced and those peaks associated with Mn^{3+} and Mn^{2+} intensified

(Fig. 5D). A shake-up satellite characteristic of Mn^{2+} also appeared after discharge. The change of the Mn oxidation states was reversed after charge, and the pristine state was regenerated (Fig. 5D; see peak assignments in table S2). Concerted with the electron transfer is the Mg^{2+} (de)intercalation, demonstrated first by reversible incorporation and extraction of 0.3 Mg^{2+} to the cathode after discharge and charge measured by inductively coupled plasma optical emission spectroscopy (table S9). Because the number of Mg^{2+} incorporated or extracted is in accord with the coulombic capacity (Fig. 5A), Mg^{2+} is the only ion that participated in the redox reaction. Unlike Mo_6S_8 and TiS_2, which demonstrate very little change of lattice indexes upon Mg^{2+} (de)intercalation (41, 42), a substantial enlargement of the interlayer distance was observed after discharging the cathode in **E4** (Fig. 5E), suggesting that larger species were intercalated with Mg^{2+}. The species were then extracted from the oxide cathode together with Mg^{2+} after the charge and the interlayer distance was reduced (Fig. 5F). The elemental distribution of the discharged cathode from energy-dispersive x-ray (EDX) spectroscopy demonstrated the presence of C and N in the materials together with Mg^{2+} (Fig. 5G), in combination with the characteristic peaks for **M4** observed in the attenuated total reflectance Fourier-transform infrared spectrum in the discharge cathode (fig. S22), confirming the presence of **M4** when an electron is transferred to the Mg^{2+} intercalated cathode. The fact that **M4** in the solvation sheath greatly facilitates the charge transfer kinetics of the cathode suggests that solvation sheath reorganization also occurs in the cathode and limits the interfacial charge transfer reaction kinetics (Fig. 5H).

The generality of the electrolyte design is demonstrated in other solvents used in RMBs such as diglyme (fig. S23) and tetrahydrofuran (fig. S24). Extension to RCBs was validated by adding **M4B** to 0.5 M calcium tetrabis(hexafluoroisopropyloxy)borate-DME, in which the Ca^{2+} plating and stripping cCE increases from 80 (43, 44) to 96% (fig. S25). **M4B** is a derivative of **M4** with an extra methylene carbon to accommodate the larger size of Ca^{2+} (fig. S26). This electrolyte was used to pair the Ca metal anode with a $Mg_{0.15}MnO_2$ full cell and demonstrates a 2.6-V average potential with a reversible capacity of 210 mA·hours g^{-1} at 0.5C for 50 cycles (fig. S27).

In this study, we identified several essential factors that are required for the cation solvation sheath to successfully undergo reorganization for a fast Mg^{2+}/Mg redox reaction, including (i) the solvation free energy for Mg^{2+} serving as a descriptor for salt dissociation, (ii) the reduction potential for the $Mg^{2+}(solvent)_n \rightarrow$ $Mg^+(solvent)_n$ reaction to ensure that the

Mg^{2+}/Mg redox occurs within the electrolyte cathodic stability window, and (iii) the reorganization free energy (λ). To discover additional chelants, several compounds were screened using DFT (fig. S16) and validated with cycling tests (fig. S27). Ethylenediamine was found as a promising chelant or solvent owing to its high free energy of solvation, high reduction potential for Mg^{2+}, and low λ.

Methoxyethyl-amines were demonstrated to circumvent commonly observed challenges such as high interfacial impedance and overpotentials for plating and stripping Mg and Ca by preferential solvation of metal cations and facilitating the initial reduction step. This approach simultaneously solved two critical challenges for divalent metal batteries: the low reversibility for anodes and sluggish kinetics of metal-oxide cathodes, enabling the energy densities of RMBs and RCBs to be comparable to that of LIBs. The design principle is generally applicable for divalent metal batteries. The reorganization energy can be tuned by tailoring the molecular structures through the introduction of heterogeneous donor atoms and less compact structures to further enhance the kinetics and reversibility to match the application standard for commercial LIBs.

REFERENCES AND NOTES

1. M. Armand, J.-M. Tarascon, *Nature* **451**, 652–657 (2008).
2. J. Muldoon, C. B. Bucur, T. Gregory, *Chem. Rev.* **114**, 11683–11720 (2014).
3. M. Li et al., *Nat. Rev. Mater.* **5**, 276–294 (2020).
4. P. Canepa et al., *Chem. Rev.* **117**, 4287–4341 (2017).
5. K. Xu, *Chem. Rev.* **104**, 4303–4417 (2004).
6. Y. Li, Y. Qi, *Energy Environ. Sci.* **12**, 1286–1295 (2019).
7. S. H. Lapidus et al., *Phys. Chem. Chem. Phys.* **16**, 21941–21945 (2014).
8. Z. Lu, A. Schechter, M. Moshkovich, D. Aurbach, *J. Electroanal. Chem.* **466**, 203–217 (1999).
9. D. Aurbach, R. Skaletsky, Y. Gofer, *J. Electrochem. Soc.* **138**, 3536–3545 (1991).
10. E. Levi, Y. Gofer, D. Aurbach, *Chem. Mater.* **22**, 860–868 (2010).
11. G. S. Gautam et al., *Chem. Commun.* **51**, 13619–13622 (2015).
12. Z. Rong et al., *Chem. Mater.* **27**, 6016–6021 (2015).
13. G. Gershinsky, H. D. Yoo, Y. Gofer, D. Aurbach, *Langmuir* **29**, 10964–10972 (2013).
14. X. Sun, V. Duffort, B. L. Mehdi, N. D. Browning, L. F. Nazar, *Chem. Mater.* **28**, 534–542 (2016).
15. L. Yu, X. Zhang, *J. Colloid Interface Sci.* **278**, 160–165 (2004).
16. J. Song, E. Sahadeo, M. Noked, S. B. Lee, *J. Phys. Chem. Lett.* **7**, 1736–1749 (2016).
17. C. B. Bucur, T. Gregory, A. G. Oliver, J. Muldoon, *J. Phys. Chem. Lett.* **6**, 3578–3591 (2015).
18. J. Muldoon et al., *Energy Environ. Sci.* **6**, 482–487 (2013).
19. K. W. Nam et al., *Nano Lett.* **15**, 4071–4079 (2015).
20. X. Ji et al., *Nano Lett.* **18**, 6441–6448 (2018).
21. S.-Y. Ha et al., *ACS Appl. Mater. Interfaces* **6**, 4063–4073 (2014).
22. N. Sa et al., *RSC Advances* **6**, 113663–113670 (2016).
23. T. J. Carter et al., *Angew. Chem. Int. Ed.* **53**, 3173–3177 (2014).
24. O. Tutusaus et al., *Angew. Chem. Int. Ed.* **54**, 7900–7904 (2015).
25. H. Dong et al., *Nat. Energy* **5**, 1043–1050 (2020).
26. Z. Zhao-Karger, M. E. Gil Bardaji, O. Fuhr, M. A. Fichtner, *J. Mater. Chem. A Mater. Energy Sustain.* **5**, 10815–10820 (2017).
27. J. T. Herb, C. A. Nist-Lund, C. B. Arnold, *ACS Energy Lett.* **1**, 1227–1232 (2016).
28. Z. Zhang et al., *Adv. Energy Mater.* **7**, 1602055 (2017).
29. J. Luo, Y. Bi, L. Zhang, X. Zhang, T. L. Liu, *Angew. Chem. Int. Ed.* **58**, 6967–6971 (2019).
30. S.-B. Son et al., *Nat. Chem.* **10**, 532–539 (2018).

31. M. Bremer, H. Noth, M. Warchhold, *Eur. J. Inorg. Chem.* **2003**, 111–119 (2003).
32. A. Xia, J. E. Knox, M. J. Heeg, H. B. Schlegel, C. H. Winter, *Organometallics* **22**, 4060–4069 (2003).
33. N. N. Rajput, X. Qu, N. Sa, A. K. Burrell, K. A. Persson, *J. Am. Chem. Soc.* **137**, 3411–3420 (2015).
34. T. Van Voorhis *et al.*, *Annu. Rev. Phys. Chem.* **61**, 149–170 (2010).
35. R. A. Marcus, *Annu. Rev. Phys. Chem.* **15**, 155–196 (1964).
36. R. A. Marcus, *J. Chem. Phys.* **43**, 679–701 (1965).
37. C. E. Chidsey, *Science* **251**, 919–922 (1991).
38. P. Bai, M. Z. Bazant, *Nat. Commun.* **5**, 3585 (2014).
39. Y.-P. Liu, M. D. Newton, *J. Phys. Chem.* **98**, 7162–7169 (1994).
40. E. R. Barthel, I. B. Martini, B. J. Schwartz, *J. Phys. Chem. B* **105**, 12230–12241 (2001).
41. E. Levi, A. Mitelman, D. Aurbach, M. Brunelli, *Chem. Mater.* **19**, 5131–5142 (2007).
42. X. Sun, P. Bonnick, L. F. Nazar, *ACS Energy Lett.* **1**, 297–301 (2016).
43. A. Shyamsunder, L. E. Blanc, A. Assoud, L. F. Nazar, *ACS Energy Lett.* **4**, 2271–2276 (2019).
44. Z. Li, O. Fuhr, M. Fichtner, Z. Zhao-Karger, *Energy Environ. Sci.* **12**, 3496–3501 (2019).

Science

Solvation sheath reorganization enables divalent metal batteries with fast interfacial charge transfer kinetics

Singyuk HouXiao JiKaren GaskellPeng-fei WangLuning WangJijian XuRuimin SunOleg BorodinChunsheng Wang

Efficient, rechargeable Mg and Ca batteries

Divalent rechargeable metal batteries such as those based on magnesium and calcium are of interest because of the abundance of these elements and their lower tendency to form dendrites, but practical demonstrations are lacking. Hou *et al.* used methoxyethyl amine chelants in which the ligands attach to the metal atom in more than one place, modulating the solvation structure of the metal ions to enable a facile charge-transfer reaction (see the Perspective by Zuo and Yin). In full battery cells, these components lead to high efficiency and energy density. Theoretical calculations were used to understand the solvation structures. —MSL

View the article online
https://www.science.org/doi/10.1126/science.abg3954
Permissions
https://www.science.org/help/reprints-and-permissions

Use of think article is subject to the Terms of service